

# Interchangeable Use of GNSS and Seismic Data for Rapid Earthquake Characterization: 2021 Chignik, Alaska, Earthquake

Revathy M. Parameswaran<sup>\*1</sup>, Ronni Grapenthin<sup>1</sup>, Michael E. West<sup>1</sup>, and Alexander Fozkos<sup>1</sup>

## Abstract

Earthquake magnitude estimation using peak ground velocities (PGVs) derived from Global Navigation Satellite Systems (GNSS) data has shown promise for rapid characterization of damaging earthquakes. Here, we examine the feasibility of using GNSS-derived velocity waveforms as interchangeable data for rapid magnitude and ground motion estimation that typically rely on strong-motion seismic records. Our study compares PGVs derived from high-rate GNSS to those computed from high-rate seismic records (strong-motion and velocity) at collocated and closely located stations. The recent 2021  $M_w$  8.2 Chignik earthquake in Alaska that was recorded on collocated GNSS and strong-motion sensors provides the perfect opportunity to compare the two data streams and their application in rapid response. The Chignik velocity records appear almost identical at collocated GNSS and strong-motion stations when observed at frequencies  $< 0.25$  Hz. GNSS and strong-motion derived velocity data are further employed to generate rapid estimates of PGV-derived moment magnitudes for the earthquake. The moment magnitude estimates from GNSS and joint GNSS and joint (GNSS and seismic) data are within  $\sim \pm 0.4$  magnitude units (Fang *et al.*, 2020) of the final magnitude ( $M_w$  8.2). ShakeMaps generated for the 2021 Chignik earthquake using GNSS and seismic PGVs show notable agreement between them, and show negligible shifts in PGV contours when collocated and closely located GNSS and seismic stations are substituted for one another. Therefore, we posit that GNSS is a powerful alternative or addition to seismic data and vice versa.

## Cite this article as

Parameswaran, R. M., R. Grapenthin, M. E. West, and A. Fozkos (2023). Interchangeable Use of GNSS and Seismic Data for Rapid Earthquake Characterization: 2021 Chignik, Alaska, Earthquake, *Seismol. Res. Lett.* **XX**, 1–12, doi: 10.1785/0220220357.

## Supplemental Material

## Introduction

### Joint approach to earthquake rapid response

Along most subduction zones, seismic risk and damage estimation associated with large earthquakes depend on rapid, accurate evaluation of earthquake magnitude, and associated ground shaking. Regions prone to high seismic risk could benefit from simultaneous (to increase accuracy) or interchangeable (in the event that either type of data are unavailable or inoperative) use of seismic and geodetic data for rapid earthquake detection and characterization. From an operational perspective for earthquake early warning, early detection using  $P$ -wave arrivals in the immediate vicinity of an earthquake is a widely used method (e.g., Given *et al.*, 2014; Kuyuk *et al.*, 2014; Rinehart *et al.*, 2016). Meanwhile, rapid earthquake characterization relies on incoming  $S$  waves, for which the focus is also on estimating the magnitude, depth, and the area of impact, accommodating for the full rupture, besides event detection (e.g., Grapenthin *et al.*, 2014a,b; 2017; Crowell *et al.*, 2016). Over the last two decades,

high-rate GNSS ( $\geq 1$  Hz) have become mature enough to detect and characterize earthquakes in real time. These high-rate GNSS position data can be used in conjunction with positions estimated by double-integrating accelerations from collocated high-rate strong-motion instruments through a Kalman filter to create displacement data streams of millimeter-scale precision (Bock *et al.*, 2011). Peak ground displacements (PGDs) derived from high-rate GNSS time series have been effectively used in rapid magnitude estimation for large earthquakes using PGD-magnitude scaling relationships (e.g., Crowell *et al.*, 2013; Grapenthin *et al.*, 2014b; Melgar *et al.*, 2016; Grapenthin *et al.*, 2017). A different approach would be to characterize earthquakes using

1. Geophysical Institute, University of Alaska Fairbanks, Fairbanks, Alaska, U.S.A., <https://orcid.org/0000-0001-7094-8436> (RMP); <https://orcid.org/0000-0002-4926-2162> (RG); <https://orcid.org/0000-0003-0387-5550> (AF)

\*Corresponding author: [rmpameswaran@alaska.edu](mailto:rmpameswaran@alaska.edu)

© Seismological Society of America

co-seismic ground velocities. This was successfully illustrated by computing instantaneous receiver velocities (or “instavels”) for large earthquakes from high-rate GNSS data (Colosimo *et al.*, 2011; Grapenthin *et al.*, 2018). The advantages of using instavels are that they can be rapidly computed using single frequency GNSS data, ultrarapid orbits, and no atmospheric or ionospheric models (Colosimo *et al.*, 2011; Grapenthin *et al.*, 2018). Akin to PGDs, peak ground velocities (PGVs) derived from instavels can also be scaled to magnitude and hypocentral distances by constraining attenuation relationships, and can be used for rapid earthquake characterization (Fang *et al.*, 2020). Grapenthin *et al.* (2018) illustrate that PGVs derived from instavels when subjected to PGV-magnitude scaling relationships can be incorporated into ground-motion products such as ShakeMaps. However, it is important to evaluate how instavels compare to strong-motion or seismic velocity observations to establish coherence between the two data types. Our hope is to provide a quantitative foundation describing the applications for which GNSS and strong-motion seismic data can be used interchangeably or in combination, and what the caveats are (e.g., PGV-derived magnitude estimates, ground-motion intensity maps, etc.). The 2021  $M_w$  8.2 Chignik earthquake provided an ideal test case to examine the interchangeability of GNSS and seismic data in rapid earthquake characterization.

The size and location of the 29 July 2021  $M_w$  8.2 Chignik earthquake in Alaska provided a rare opportunity to reconcile GNSS observations with their seismic counterparts. The earthquake was the largest event in more than 50 yr along the Aleutian megathrust, and the earthquake epicenter was in the vicinity of collocated or closely located GNSS and seismic stations, inducing signals well above the noise floor of the observing instrumentation. In this article, we examine geodetic and seismic velocity records of the earthquake and how they compare. Furthermore, we assess the relationship between hypocentral distance and PGVs with the rapid magnitude estimates derived from both GNSS and seismic velocities. Finally, we explore the effectiveness of GNSS observations as an alternate and complementary dataset that can be incorporated into ground-motion estimation products. The ground-motion models can be generic or region specific; an example of the latter would be those used in Japan, for instance (e.g., Koketsu *et al.*, 2008; Morikawa and Fujiwara, 2013). In this study, we model ground motion using the ShakeMap program (Worden *et al.*, 2012).

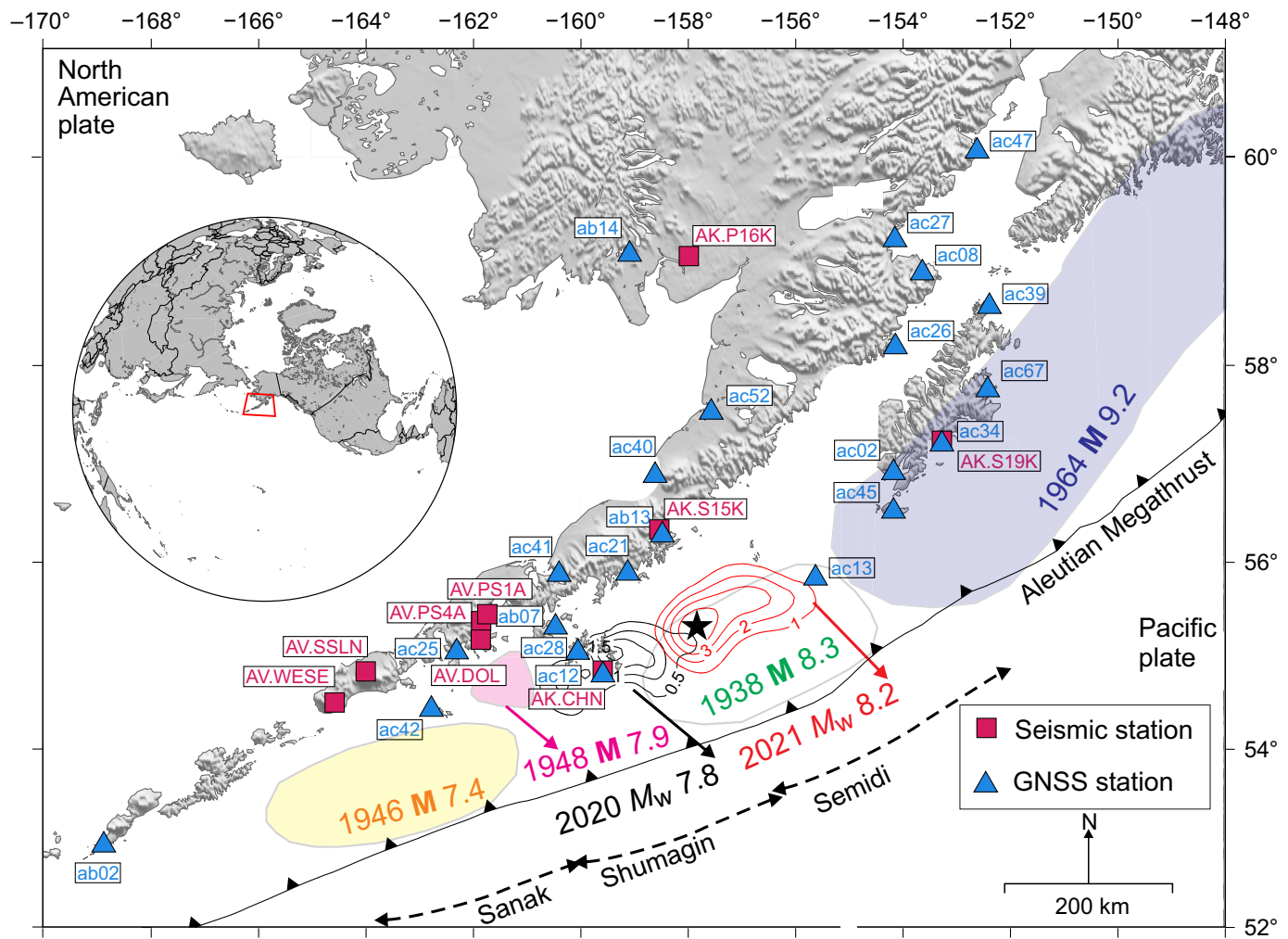
### The 2021 $M_w$ 8.2 Chignik earthquake

The 2021  $M_w$  8.2 Chignik earthquake in Alaska was the largest earthquake in the United States since the 1965  $M$  8.7 Rat Island event (Stauder, 1968; Wu and Kanamori, 1973; Elliott *et al.*, 2022). The earthquake occurred along the Alaska–Aleutian subduction zone, where the Pacific plate underthrusts the North American plate. The subduction zone is noted for its high-seismic productivity and variable coupling (e.g., Sykes

*et al.*, 1981; Drooff and Freymueller, 2021) (Fig. 1). Segments of the subduction arc close to the Alaskan Peninsula, and the eastern Aleutian Islands have witnessed several large earthquakes in recorded history. The 1964  $M$  9.2 Prince William Sound earthquake (e.g., Ichinose *et al.*, 2007; Benz *et al.*, 2011), the 1938  $M$  8.3 Alaska Peninsula earthquake (e.g., Johnson and Satake, 1994), and the 1946  $M$  7.4 Sanak earthquake ( $M$  8.6 based on the magnitude of the ensuing tsunami) (e.g., López and Okal, 2006) are a few of the larger events to strike this subduction zone. However, the area stretching across the Shumagin Islands, sandwiched between the 1938 and 1946 events, does not have a clear history of great earthquakes and has been known as the “Shumagin seismic gap” (Davies *et al.*, 1981; Witter *et al.*, 2014). This is no longer the case, since the 22 July 2020  $M_w$  7.8 Simeonof earthquake ruptured deeper portions of the megathrust below the continental shelf (Crowell and Melgar, 2020; Liu *et al.*, 2020; Xiao *et al.*, 2021; Ye *et al.*, 2021). To its east-northeast, the Simeonof event was followed by the 2021  $M_w$  8.2 Chignik earthquake, which seems to have ruptured the western two-thirds of the 1938 Alaska Peninsula earthquake aftershock zone, with little evidence of it being a repeat of the 1938 event (Elliott *et al.*, 2022; Liu *et al.*, 2022; Ye *et al.*, 2022). Together with the 2020 Simeonof earthquake, the Chignik event seems to have closed the deeper parts of the Shumagin gap (Elliott *et al.*, 2022). We choose the 2021 Chignik earthquake in this study because of (1) the size of the earthquake and associated ground motions, (2) the proximity to functional and well-maintained seismic and geodetic networks, and (3) most importantly, the existence of collocated seismic and geodetic stations.

### Methodology and Results

We start by identifying GNSS stations that continuously recorded high-rate data during the Chignik earthquake and are located within 600 km from the epicenter. The GNSS instrumentation comprises stations that operate at 1 and/or 5 Hz sampling rate, of which we use the 1 Hz data for consistency in analysis. We then proceed to select seismic stations that are collocated or closely located to the GNSS stations identified here. The seismic instrumentation comprises two types: broadband and strong-motion. The broadband sensors are weak-motion instruments designed to record small ground motions with high signal-to-noise and high fidelity across a wide range of frequencies. Broadband data are natively recorded in velocity. However, the strong ground motions near large earthquakes exceed the dynamic range and amplitude limits of most broadband sensors. To help account for this, strong-motion accelerometers are deployed to complement broadbands. Most strong-motion sensors record natively in acceleration. Within the defined bounds, three strong-motion stations (AK.S15K, AK.CHN, and AK.S19K) are collocated and closely located to three of the selected GNSS receivers (AB13, AC12, and AC34). Of the



operational GNSS and strong-motion stations, two pairs are collocated, whereas another is closely located (<2 km). There are several broadband stations (for e.g., AV.DOL, AK.P16K, AV.PS1A, AV.PS4A, AV.SSLN, AV.WESE, etc.) that are at comparable hypocentral distances as the GNSS stations. However, we primarily focus on the strong-motion records to avoid data saturation in broadband velocity data (Fig. S1, available in the supplemental material to this article).

Traditionally, GNSS data are considered in displacement space, while strong-motion sensors natively record in acceleration. We choose to compare the datasets in velocity space for a number of reasons. Unlike position data, GNSS receiver velocities or instavels can be estimated directly from GNSS satellite phase and range observations. This reduces the complexity arising from multiple time derivatives and externally obtained corrections (Misra and Enge, 2011), resulting in records without amplitude saturation (unlike seismic velocity records) from these noninertial sensors. Double integrating strong-motion acceleration records to produce displacement is problematic, because the static integration term (arguably the core strength of GNSS) is lost. Finally, the comparatively low, currently prevalent sample rate of GNSS (1 Hz) means that frequencies above 0.5 Hz are not recorded. This impact would be exacerbated by

**Figure 1.** Seismic and Global Navigation Satellite Systems (GNSS) station coverage for the 2021  $M_w$  8.2 Chignik earthquake. The limits for the 1964  $M$  9.2 Prince William Sound, 1938  $M$  8.3 Semidi, 1946  $M$  7.4 Sanak (or Unimak), and the 1948  $M$  7.9 Shumagin earthquakes are based on Davies *et al.* (1981). The 0.5 m slip contours for the 2020  $M_w$  7.8 Simeonof earthquake are based on Xiao *et al.* (2021), and the 1 m slip contours for the 2021  $M_w$  8.2 Chignik earthquake are as estimated by Elliott *et al.* (2022). This study analyzed data from 22 GNSS and three strong-motion stations (AK.CHN, AK.S15K, and AK.S19K). Figure also shows some of the other broadband stations in the vicinity of the earthquake but are not used in this study due to amplitude saturation. This is the band used for the frequency filter. The inset in the figure shows the location of the study region on the globe. The color version of this figure is available only in the electronic edition.

differentiating the GNSS to acceleration. For these reasons, velocity provides a middle ground for comparing these data that minimizes the caveats on both the data types.

### Instantaneous GNSS velocities: instavels

Instantaneous GNSS receiver velocities or instavels are derived from the Doppler shift observed in the carrier phase change that results from both satellite and receiver motion. When

the satellite trajectory is smooth or well known (e.g., Benedetti *et al.*, 2014; Grapenthin *et al.*, 2018), the change in the observed frequency of the satellite signal primarily represents the receiver velocity (Misra and Enge, 2011). Phase-velocity (Doppler shift) observations for a GNSS receiver are computed assuming that ionosphere and troposphere are static over short-time periods ( $\leq 1$  s), and no cycle slips occur (Misra and Enge, 2011; Gaglione, 2015). We can infer this from differenced subsequent carrier phase observations  $\Delta\phi^s$ :

$$\Delta\phi^s = (\mathbf{v}^s - \mathbf{v}_r) \times \mathbf{l}^s + \hat{b} + \delta\epsilon_\phi, \quad (1)$$

in which  $(\mathbf{v}^s - \mathbf{v}_r) \times \mathbf{l}^s$  is the range difference between the velocity  $\mathbf{v}^s$  of satellite  $s$ , which is known and can thus be removed, and velocity  $\mathbf{v}_r$  of receiver  $r$ , is projected onto the receiver-to-satellite line of sight with the respective unit vector  $\mathbf{l}^s$ . The terms  $\hat{b}$  and  $\delta\epsilon_\phi$  are the shifts in satellite and receiver clock biases and error terms, respectively. The Doppler shifts observed from at least four satellites due to the receiver moving at velocity  $\mathbf{v}_r$ , is given by

$$\mathbf{D} = \mathbf{G}[\mathbf{v}_r \hat{b}_r]^T + \delta\epsilon_\phi, \quad (2)$$

in which  $\mathbf{D}$  is a vector of Doppler shift observations, and  $\mathbf{G}$  is the system matrix that contains unit vectors to project the receiver velocities  $\mathbf{v}_r = [v_x v_y v_z]^T$  onto the line of sight to the satellite. The instavels are calculated in an Earth-centered, Earth-fixed Cartesian coordinate system and then rotated into a local east–north–up reference frame. Equation (2) is solved for  $V_r$  and  $\hat{b}_r$  (receiver clock bias) using standard least-squares techniques (e.g., Aster *et al.*, 2018), and observation weights are removed based on satellite elevation angles in the inversion. We consider and compare observations from a combination of L1 (1575.42 MHz) and L2 (1227.6 MHz) transmission frequencies, and using L2 alone.

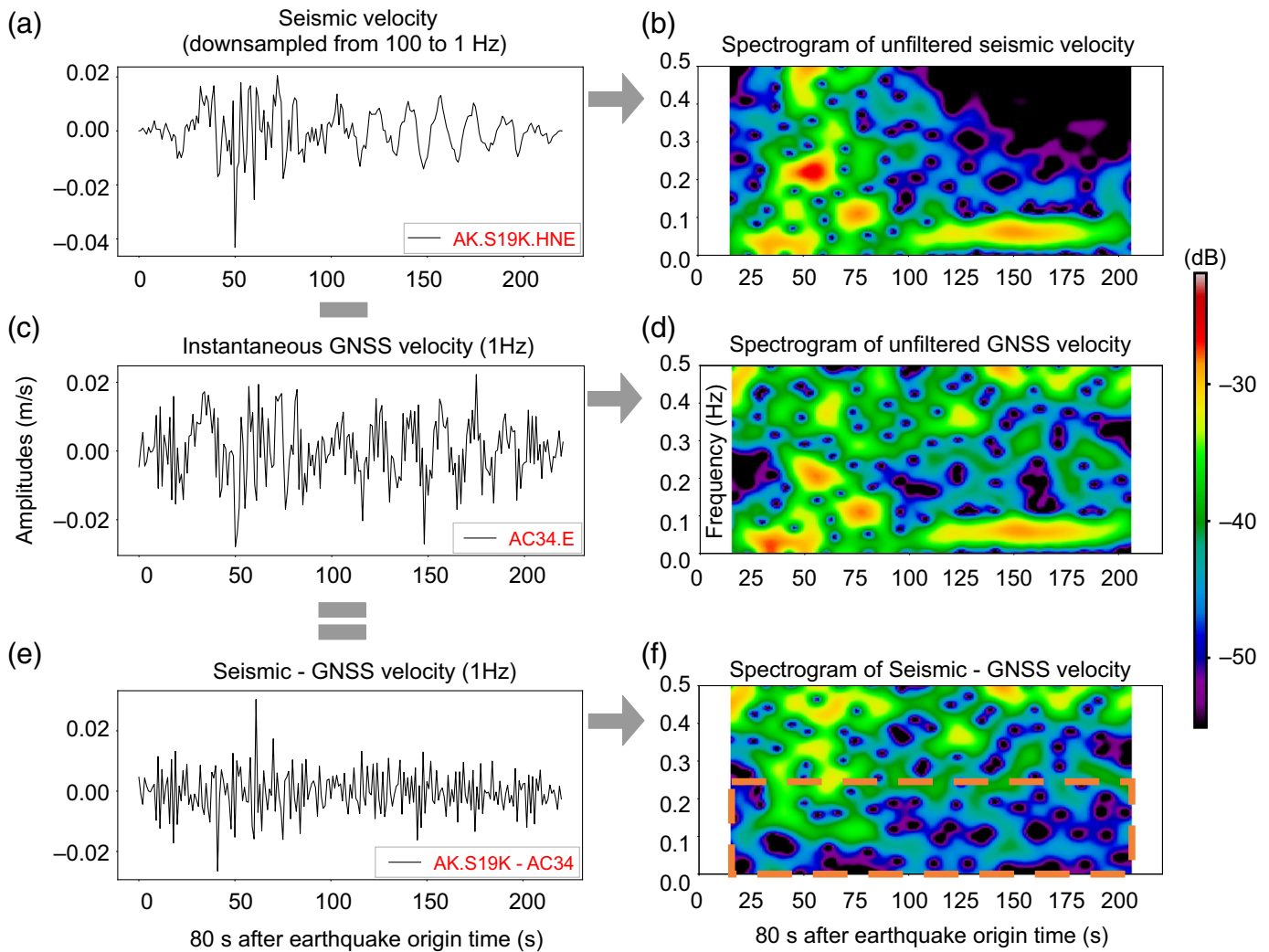
### Seismic versus instavel comparison for collocated stations

The GNSS data used in the study are limited to 1 Hz sampling rates, whereas seismic data are sampled at 50–100 Hz. To facilitate direct comparison, we resample the seismic data to a common sampling rate (1 Hz). We achieve this by correcting for instrument response in the seismic data followed by resampling it to the 1 Hz GNSS timestamps using the ObsPy framework (Beyreuther *et al.*, 2010; Megies *et al.*, 2011; Krischer *et al.*, 2015). We use Coordinated Universal Time (UTC) timestamps for the seismic data. The UTC is defined based on atomic clocks, and the corrections associated with Earth’s rotation are incorporated into them. Meanwhile, the clocks on Global Positioning System (GPS) satellites, which we use to procure GNSS data for this study, were calibrated to UTC in 1980 but do not account for corrections from that point

onward. Therefore, integer corrections called “leap seconds” are introduced at appropriate times to account for variations from UTC (e.g., Lewandowski and Arias, 2011). Here, the GNSS data are time shifted by +18 s for the year 2021. At the “seconds” mark, the raw GNSS and seismic timestamps deviate from one another by an order of  $1 \times 10^{-3}$  s. This deviation is considerably lower than the individual sampling rates. Therefore, we neglect this difference instead of accounting for the deviation through interpolation approaches. The strong-motion data are subsequently subjected to trapezoidal first-order integration using ObsPy to obtain corresponding velocities.

The resampled seismic velocity traces are then compared to their GNSS instavel counterparts with the objective of identifying (a) commonalities that represent the Chignik earthquake and (b) the frequencies at which the GNSS produce faithful ground-motion records for this event. We start by subtracting the seismic time series from the GNSS instavels (Fig. 2e). Subsequently, we generate spectrograms for each of the time series—seismic, instavel, and differenced records—as illustrated in Figure 2b,d,f. The spectrograms allow us to identify frequency bands with common energy distributions. For the station pair AC34 (GNSS) and AK.S19K (strong-motion) (henceforth identified as station pair AC34:S19K—GNSS: strong-motion), we observe highly similar signals within the frequency range 0.001–0.25 Hz. However, at frequencies above  $\sim 0.25$  Hz we observe energy in the instavels that does not appear in the strong-motion record. We attribute this to spurious noise in the GNSS data. The spectrogram of the signal difference (Fig. 2f) further confirms that the two signals are most similar below 0.25 Hz. To examine the coherence of the signal that is common to both records, we band-pass filter the data at 0.001–0.25 Hz (Fig. 3a–f) and then cross correlate the filtered time series (Fig. 3h–i, bottom). The peak of the cross-correlation function provides an objective measure of similarity. The lag time associated with the cross-correlation peak reveals whether or not the processing introduces meaningful time shifts (Fig. 3a–i).

We apply this method to the two other collocated GNSS–seismic station pairs—AC34:S19K (Figs. 2, 3) and AC12:CHN (Fig. S2), and closely located stations AB13:S15K that are separated by  $\sim 2$  km (Fig. S3). These three comparisons suggest that a large portion of the Chignik earthquake signal is captured in the GNSS records in the 0.001–0.25 Hz frequency band (Figs. 2, 3; Figs. S2, S3). Collocated stations AC34:S19K show a high correlation of 0.9 and a lag of  $-1$  s (east component) (Fig. 3a). The second pair of collocated stations AC12:CHN show a correlation of 0.77 and a lag of  $-1$  s (Fig. S2). Closely located stations AB13:S15K show a wider range of frequency content in their spectrogram and show lower correlation (cross-correlation = 0.6; lag = 0 s) compared to the collocated stations (Fig. S3).



### PGV-derived magnitude: GNSS, seismic, joint

Fang *et al.* (2020) proposed a method to estimate earthquake magnitudes using PGVs derived from instavels. They developed attenuation relationships for PGVs with respect to hypocentral distances using over 1434 records from 22 earthquakes worldwide. They used these attenuation relationships to constrain an empirical PGV-magnitude scaling law. The 3D or 2D (horizontal only) PGV from a three-component instavel waveform is given by

$$PGV_{\text{total}} = \max(v_n^2 + v_e^2 + v_u^2)^{1/2}, \quad (3)$$

$$PGV_{\text{horizontal}} = \max(v_n^2 + v_e^2)^{1/2}, \quad (4)$$

in which  $v_n$ ,  $v_e$ , and  $v_u$  are the north, east, and up velocity waveforms, respectively.

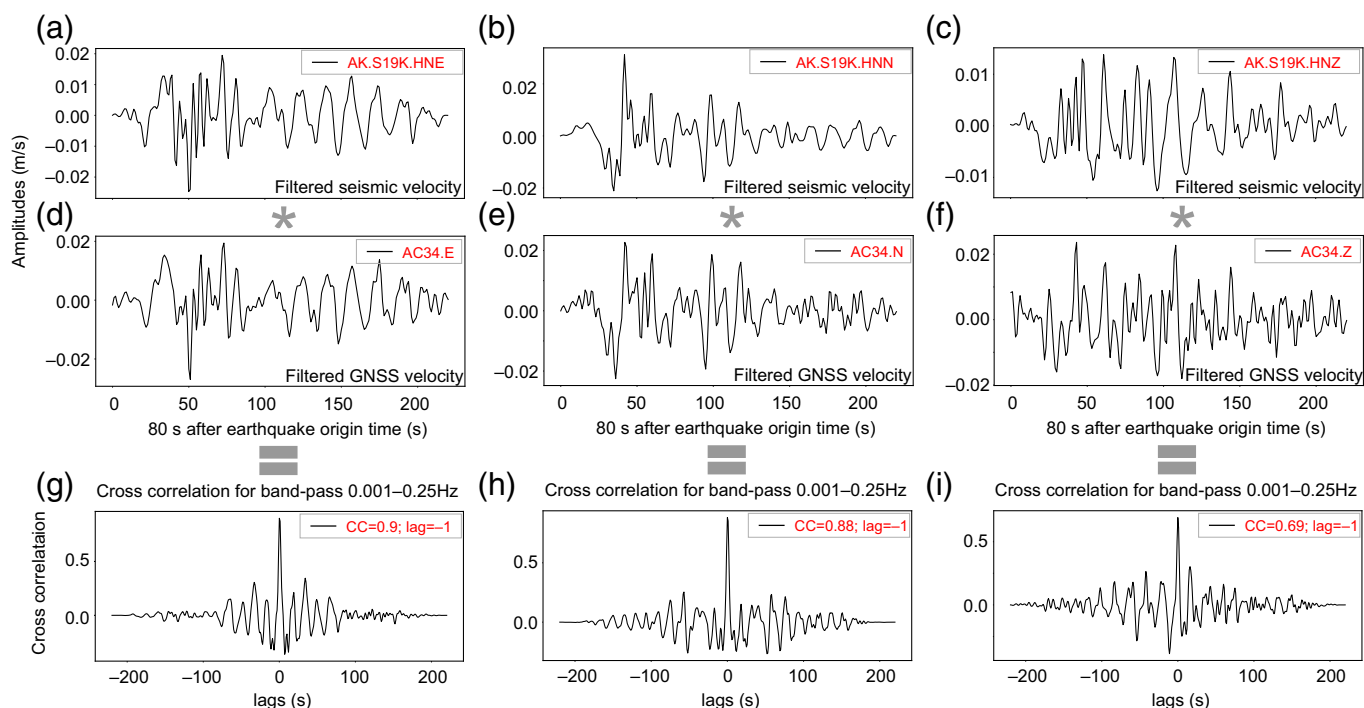
Fang *et al.* (2020) formulated the moment magnitude ( $M_w$ ) calculation based on the following scaling law between PGVs and hypocentral distances ( $R$ ):

$$\log(PGV) = A + B \times M_w + C \times M_w \times \log(R), \quad (5)$$

**Figure 2.** Collocated GNSS versus strong-motion station pair for the 2021 Chignik earthquake. (a) Resampled (100 to 1 Hz) and unfiltered east seismic velocity time series from strong-motion station AK.S19K. (b) Spectrogram of strong-motion-derived velocity from AK.S19K. (c) Unfiltered east component of instavel from GNSS station AC34. (d) Spectrogram of AC34 instavel. (e) Time series of GNSS noise obtained by differencing the GNSS and the seismic velocity time series. (f) Spectrogram of subtracted frequency time series. The orange box in panel (f) highlights the frequency range in which the two signals show strong coherence. This is the band used for the frequency filter. The color version of this figure is available only in the electronic edition.

in which  $A = -5.025 \pm 0.084$ ,  $B = 0.741 \pm 0.017$ , and  $C = -0.111 \pm 0.003$  are the regression coefficients, and the standard deviation of the magnitude residual (predicted minus actual magnitudes) is  $\pm 0.389$  ( $\sim \pm 0.4$ ) magnitude units.

We produce PGVs from the unfiltered (up to 0.5 Hz; Nyquist frequency for 1 Hz sampling) seismic and GNSS velocity time series (Table 1), and implement the Fang *et al.* (2020) PGV scaling relationships for magnitude estimation for the 2021



Chignik earthquake. To simulate a real-time environment, we recalculate PGV at each timestep, effectively creating PGV time series that monotonically increases toward the global PGV for each station (listed in Table 1) and remains constant after that. Using these PGV time series, we determine the moment magnitude evolution from instavels and seismic PGVs individually, and as a combined dataset (GNSS + seismic). For an effective comparison, we first compute rapid estimates of magnitude using all 22 GNSS stations (UNAVCO Community 2004a,b, 2005, 2006a,b,c,d,e,f,g,h, 2007a,b,c,d,e,f,g, 2008a,b,c,d), followed by magnitude estimates using the strong-motion stations alone, and then using both GNSS (22) and strong-motion (three) stations. The instavels are computed using L2 and L1 + L2 frequency bands, of which we prefer to use the results obtained using the L2 frequencies (Fig. 4) due to the larger noise levels in L1 frequencies, although the final magnitude estimates are comparable. Figure 4a shows the evolution of moment magnitude from instavels (22 stations; L2 and L1 + L2), strong-motion (three stations), and combined data (22 instavels and three strong-motion records), with moment release over time. Figure 4b represents the scaling relation between the hypocentral distances and the GNSS and strong-motion PGVs (Table 1) for the estimated moment magnitude. PGVs obtained from all 22 GNSS stations result in a final moment magnitude of  $M_w$  8.06 (using L2;  $M_w$  7.97 using L1 + L2), within uncertainty bounds of  $\sim\pm 0.4$  magnitude units from the final magnitude ( $M_w$  8.2), as prescribed by the scaling relationships. The PGVs from strong-motion records result in a final value of  $M_w$  7.78, whereas the joint GNSS (22 stations) and strong-motion (three stations) moment magnitude arrives at  $M_w$  7.9. Based on results from GNSS and

**Figure 3.** Cross correlations for east, north, and vertical components for AC34:S19K. (a,d) East components of AK.S19K and AC34, respectively, filtered using Butterworth band-pass 0.001–0.25 Hz; (b,e) Filtered north components of AK.S19K and AC34; and (c,f) Filtered vertical components of AK.S19K and AC34. Cross-correlation between filtered components of AK.S19K and AC34 (g) east, (h) north, and (i) vertical. The color version of this figure is available only in the electronic edition.

strong-motion stations, the PGV-derived moment magnitudes are within the predicted standard deviations ( $\sim\pm 0.4$ ) of magnitude units (Fang *et al.*, 2020).

### GNSS and seismic ShakeMaps

We use the operational ShakeMap configuration (Worden *et al.*, 2012) at the Alaska Earthquake Center to assess the possibility of using instavels as an alternative or in addition to seismic input for ShakeMaps. The ShakeMap methodology uses location-specific ground-motion models to forward model estimated shaking. Instrumental records are then used to adjust and correct these estimates. The more instrumental observations that are incorporated into ground-motion products, the more accurate and precise the output is. These instrumental records may comprise peak ground accelerations and/or PGVs. We compare ShakeMaps generated using instavel PGVs to those obtained from the filtered seismic velocities. ShakeMaps, as produced at the Alaska Earthquake Center are based on 0.1 Hz high-pass filtered seismic records to compute the shaking intensity and PGV contours. We further use ShakeMap to derive PGV contours using PGVs (Table 1) from identically sampled GNSS and seismic records.

TABLE 1

**GNSS and Seismic PGVs**

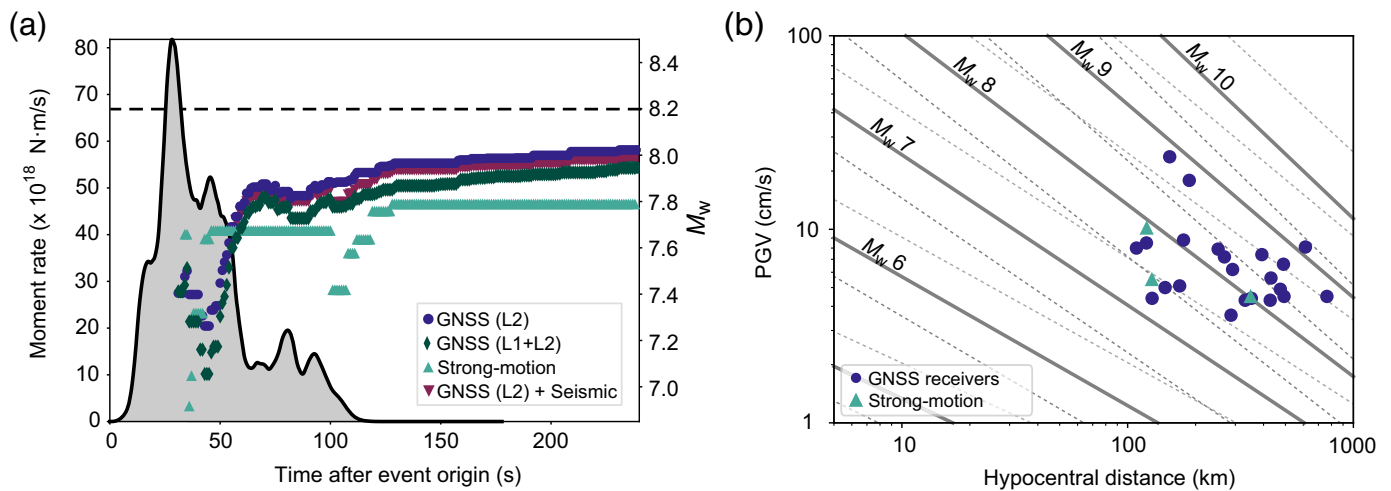
<b>Hypocentral Distance (km)</b>	<b>GNSS Station</b>	<b>Latitude (°N)</b>	<b>Longitude (°E)</b>	<b>PGV Total (cm/s)</b>	<b>PGV Horizontal (cm/s)</b>
109.6	AC21	55.921	-159.128	8.0	5.8
121.32	AB13	56.307	-158.504	8.5	8.1
128.58	AC12	54.831	-159.590	4.4	3.0
146.82	AC28	55.078	-160.049	5.0	3.3
153.88	AC13	55.822	-155.622	23.7	20.6
170.35	AB07	55.349	-160.477	5.1	4.9
177.2	AC41	55.909	-160.407	8.8	6.9
187.92	AC40	56.930	-158.619	17.9	17.9
252.28	AC52	57.567	-157.574	7.9	6.8
268.98	AC45	56.564	-154.181	7.2	6.8
287.74	AC25	55.089	-162.314	3.6	2.5
292.37	AC02	56.951	-154.183	6.2	4.7
332.5	AC42	54.472	-162.784	4.3	2.0
354.04	AC34	57.220	-153.279	4.4	3.3
394.21	AC26	58.215	-154.150	7.4	3.2
429.22	AB14	59.108	-159.092	4.3	2.2
432.58	AC67	57.791	-152.425	5.6	2.9
475.92	AC08	58.929	-153.645	4.9	2.3
491.29	AC27	59.253	-154.163	6.6	3.3
494.27	AC39	58.610	-152.394	4.5	2.4
614.73	AC47	60.081	-152.624	8.1	3.3
765.57	AB02	52.971	-168.855	4.5	2.0
<b>Hypocentral Distance (km)</b>	<b>Seismic Station</b>	<b>Latitude (°N)</b>	<b>Longitude (°E)</b>	<b>PGV Total (cm/s)</b>	<b>PGV Horizontal (cm/s)</b>
121.99	S15K	56.306	-158.540	10.1	6.9
128.58	CHN	54.831	-159.590	5.5	4.6
353.79	S19K	57.223	-153.288	4.5	4.3

Figure 5 presents PGV contours generated from: (a) 1 Hz collocated and closely located GNSS instavels (three records), (b) downsampled 1 Hz collocated and closely located strong-motion data (three stations), (c) 1 Hz GNSS instavels (22 records), and (d) 1 Hz GNSS instavels replaced with collocated and closely located downsampled strong-motion data. The corresponding ShakeMaps (with color gradients instead of the PGV contours) and the official ShakeMap released by U.S. Geological Survey (USGS) can be found in Figure S4. We observe that the PGV contours derived from the collocated and closely located GNSS and strong-motion stations are more-or-less identical (Fig. 5a,b). Meanwhile, the 20 cm/s PGV contour synthesized using all 22 instavels (Fig. 5c) shrinks by ~50 km from those generated using the three

strong-motion stations (Fig. 5a). The 10 cm/s contour also shows some shrinkage, albeit lesser, in the instavel PGVs compared to their seismic counterparts. Meanwhile, PGVs contours <10 cm/s (>200 km from the epicenter) for both cases mimic one another remarkably. The test cases illustrated in Figure 5d show that substituting GNSS stations with collocated and closely located strong-motion stations, and potentially vice versa, result in negligible changes in the extents of the PGV contours compared to the original, unsubstituted sets (Fig. 5c).

## Discussion

One of the key observations from this study is that the seismic and GNSS PGVs closely correlate at GNSS frequencies (the frequency band at which the GNSS time series effectively records

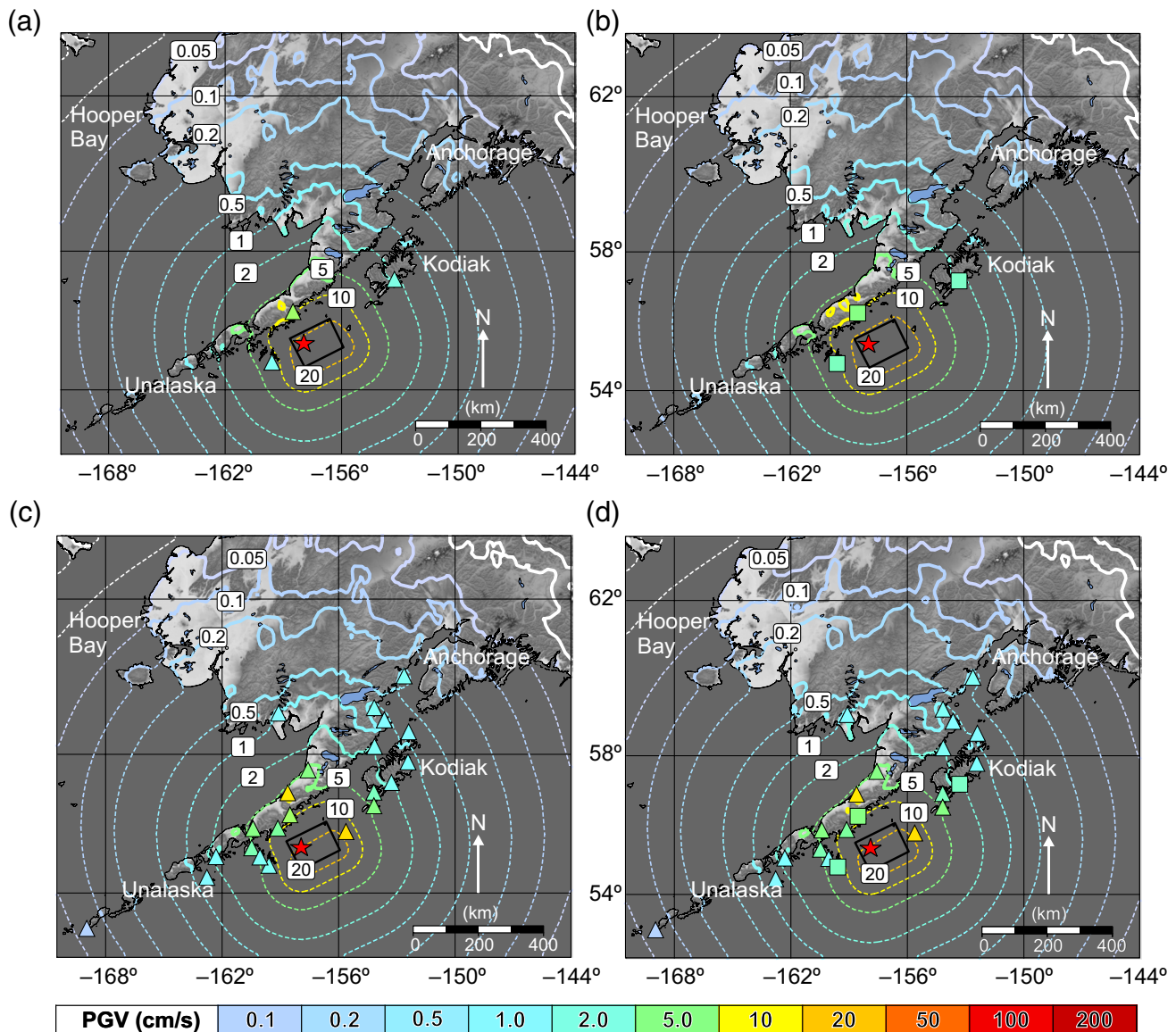


**Figure 4.** PGV-inferred moment magnitudes and scaling relationships. (a) Evolution of PGV-inferred moment magnitudes with net moment release associated with the 2021  $M_w$  8.2 Chignik earthquake. PGV-inferred moment magnitudes from GNSS (L2) = 8.06, GNSS (L1 + L2) = 7.97, strong-motion = 7.78, and joint = 7.9. The gray area marked by the curves indicates the moment release associated with the Chignik earthquake over time (from U.S. Geological Survey [USGS]). (b) PGV versus hypocentral distance plot scaled with corresponding moment magnitudes from 22 GNSS receivers and three strong-motion stations. Thick oblique lines are the predicted magnitudes as a function of PGVs and hypocentral distance based on Fang et al. (2020), whereas the dashed lines are the limits of the same. The color version of this figure is available only in the electronic edition.

ground motion with fidelity; in this case, 1 Hz data) at collocated stations for the 2021  $M_w$  8.2 Chignik earthquake. This is evident from Figures 2 and 3 that compare the AC34 instavel to the seismic trace from AK.S19K. The spectrograms of the unfiltered 1 Hz velocity time series show comparable energy distribution <0.25 Hz. A similar energy concentration was found in the case of the second collocated station pair, AC12:CHN, and the resultant correlation between the filtered data is also high (Fig. S2). Meanwhile, closely located station pair AB13:S15K, for which the stations are separated by  $\sim 2$  km, show some difference in signal and lower cross-correlation compared to the collocated stations. An examination of the sites where these stations are deployed revealed that the difference in the spectrograms is likely due to site effects caused by the  $\sim 2$  km offset (Fig. S5). Therefore, for the purposes of a study such as this, where we investigate whether collocated GNSS and seismic stations detect comparable ground motion, it is important to select those that have the same location and base. However, based on our results, we infer that seismic and GNSS stations within a given region will contain the same seismic signature in the event of an earthquake. This offers the potential for their joint or interchangeable use in rapid earthquake characterization.

Further, we find that the PGV-derived moment magnitude using GNSS, seismic, and joint data within GNSS frequency bands are well within the uncertainties estimated by Fang et al. (2020). The evolution curves using GNSS data (L1 + L2, L2) show clear jumps in the magnitude as contributions from individual stations come in (Fig. 4a). The magnitude evolution using strong-motion data also follows a similar trend as the GNSS data with the magnitude evolving at comparable times during the course of the earthquake. However, the final magnitude and smoothness of the curve are limited by the number of relevant strong-motion stations for this event. The joint dataset shows a nearly identical style of magnitude evolution as that of the GNSS data, further pointing to interchangeable and joint use of GNSS and seismic data for rapid characterization of an earthquake.

Another important observation is the difference between the absolute magnitudes of instavel- and seismic-PGVs in the near field. We find that GNSS frequencies exploited in this study do not reflect the near-field high-frequency ground motion (e.g., Grapenthin et al., 2018). This is best illustrated in the collocated GNSS and strong-motion pair AC12 (GNSS) and AK.CHN (strong-motion). Despite their location and similarity in deployment—both located atop a cliff (see Data and Resources) a few meters apart, the total PGV observed at AK.CHN (5.5 cm/s) is larger than that at AC12 (4.4 cm/s) (Table 1), although the overall cross-correlation of the full signal is good (e.g., east-component cross-correlation = 0.77; lag = -1; Fig. S2). This near-field disparity evens out the farther we move from the epicenter, at distances of >200 km. Station pair AC34 (GNSS; total PGV = 4.4 cm/s): AK.S19K (strong-motion; total PGV = 4.5 cm/s) (Table 1), collocated at  $\sim 300$  km from the hypocenter, vividly illustrate the GNSS and seismic PGVs equalizing over larger distances (e.g., east-component cross-correlation = 0.9; lag = -1; Fig. 2a,c,e). Differences in PGV amplitudes at closely located stations can also be explained by site effects, as is evident in the case of GNSS station AB13 and strong-motion station AK.S15K (see Figs. S3 and S5, Table 1). AB13 is located at the edge of a cliff, whereas AK.S15K is located  $\sim 2$  km inland from the cliff. It



follows that the two time series show lower coherence than those of collocated pairs (e.g., east-component cross-correlation = 0.6; lag = 0; Fig. S2a). Despite the fact that both stations lie at similar azimuths from the epicenter and are separated by a short distance, near-field and site effects can result in substantially different time series.

This difference in PGV amplitudes with distance is best reflected in the ShakeMaps products (Fig. 5, Fig. S4). The PGV contours generated using instavels show a slightly narrower band for the 20 cm/s excitation (Fig. 5a), whereas the corresponding band in the resampled seismic PGVs extends farther in the direction away from the trench (Fig. 5b). The near-field mismatch between GNSS and seismic PGVs could either be caused by the relatively lower sampling rates in GNSS measurements and/or differences in station deployment (e.g., AB13:S15K). However, GNSS efficiently captures far-field motion (>200 km), despite the 1 Hz data failing to capture the high-frequency content that remains focused in the near field

**Figure 5.** Peak ground velocity (PGV) contour estimates from the 2021  $M_w$  8.2 Chignik earthquake from different data sources: (a) PGV contours (dashed and solid colored lines) based on instavels from GNSS stations (AB13, AC12, and AC34). (b) Contours using velocity data from the three corresponding collocated and closely located strong-motion stations (AK.S15K, AK.CHN, and AK.S19K). (c) PGV contours using 22 instavels that were employed for rapid magnitude estimation for the 2021 Chignik earthquake. (d) PGV contours based on 22 GNSS locations with three of them replaced by corresponding collocated and closely located strong-motion stations. The numbers indicated inside the white boxes on the contours indicate the PGVs in centimeters per second. Triangles represent GNSS stations. Squares represent strong-motion stations. Red star represents the 2021 Chignik epicenter. Black rectangle shows the bounds of the fault plane. The color version of this figure is available only in the electronic edition.

and attenuates with distance (e.g., Grapenthin *et al.*, 2018). The collocated and closely located GNSS and strong-motion PGVs result in nearly identical ground-motion contours, except for small variations in the near field as stated previously (Fig. 5a,b). Similarly, when the three GNSS stations in Figure 5c are substituted with corresponding collocated and closely located strong-motion stations, we find that the resultant PGV contour output is largely unaltered (Fig. 5d). This test using collocated and closely located GNSS and strong-motion stations clearly illustrates that similarly sampled and processed GNSS and seismic data result in comparable ground-motion estimates. Therefore, continuing work is focused on how best to leverage these data for use in products such as the ShakeMap.

Although GNSS is capable of characterizing the earthquake comparably to that from seismic records, their current operational sampling rates are at least an order or two smaller than their seismic counterparts. Globally, GNSS receivers largely sample at 1 Hz, although there is a systematic growth toward employing 5 and 10 Hz sampling receivers, mainly limited by telemetry considerations. At reasonable distances away from areas of high-energy (frequency) release, employing GNSS-derived PGVs for earthquake rapid estimation is useful and easy to implement, because it is readily adaptable to work on real-time data streams and requires only short-term stable station monumentation, making it useful for rapid, large-scale deployments. The resulting velocities could be integrated into source modeling algorithms, which could prove useful in regions that have limited seismic coverage. Similarly, the install rapid characterization approach can be applied to seismic data in regions where there is readily available, functional seismic network even if there is a dearth of GNSS deployments. Therefore, PGVs derived from GNSS and seismic devices are capable of substituting one another and/or working in tandem, depending on data availability and sampling, and could also be used jointly as illustrated in our study.

## Conclusions

This study in the context of the 2021  $M_w$  8.2 Chignik earthquake illustrates that collocated seismic and GNSS records are quite similar to one another for this earthquake. This demonstrates the potential to use them as interchangeable datasets or in combination for ground-motion estimation (for instance, in ShakeMaps). We employed 1 Hz GNSS and resampled seismic data to identify the 2021  $M_w$  8.2 Chignik earthquake within the frequency range of 0.001–0.25 Hz. PGVs obtained using 1 Hz GNSS and seismic data were used to generate rapid estimates of PGV-derived moment magnitudes for the earthquake. We find that the estimates from GNSS and joint GNSS and joint (GNSS and seismic) data result in values within  $\sim\pm 0.4$  magnitude units of the final magnitude of  $M_w$  8.2. This agrees with PGV, hypocentral distance, and moment magnitude scaling relationship prescribed by Fang *et al.* (2020). The PGVs derived from seismic data slightly underestimate the moment

magnitude, although this could be attributed to the scaling relationships that were defined primarily using GNSS data.

Meanwhile, ShakeMaps generated using the GNSS and seismic PGVs provide important insights into the conditions under which GNSS could be used as an alternative to or jointly with seismic data. We observe that, in the case of the 2021 Chignik earthquake, GNSS and seismic PGVs are nearly identical when near-field, collocated and closely located GNSS and strong-motion stations are employed. We also note that substituting collocated GNSS and seismic stations with another introduces negligible changes in the extents of the PGV contours. However, GNSS underestimates near-field ground motion compared to neighboring seismic stations at distances <200 km from the epicenter. We believe that this is a direct consequence of differences in sampling rates between the 1 Hz GNSS receiver and the 50 or 100 Hz seismic station. It is likely that the GNSS receiver, operating at a lower sampling rate, fails to record larger ground motion at higher frequencies. Therefore, the first step to incorporating GNSS data into ShakeMap generation would be to mitigate for differences in observations due to sampling mismatch.

## Data and Resources

Seismograms and related metadata used in this study were obtained from the Alaska Earthquake Center (doi: 10.7914/SN/AK). The facilities of Incorporated Research Institutions for Seismology (IRIS) Data Services (<https://service.iris.edu>, last accessed June 2022), and specifically the IRIS Data Management Center (DMC), were used for access to these waveforms, related metadata, and/or derived products used in this study. The Global Navigation Satellite Systems (GNSS) data used here can be procured from University NAVSTAR Consortium (UNAVCO) at [unavco.org](http://unavco.org), and the associated references are cited in this article. The codes used are cited in the article. Additional information to this article can be found in the supplemental material. Station specific data for Global Positioning System (GPS) and seismic stations were obtained from <https://www.unavco.org/instrumentation/> (last accessed in February 2022) and <https://earthquake.alaska.edu/network> (last accessed in February 2022), respectively.

## Declaration of Competing Interests

The authors acknowledge that there are no conflicts of interest recorded.

## Acknowledgments

Revathy M. Parameswaran and Ronni Grapenthin were supported through the National Aeronautics and Space Administration (NASA) Earth Surface and Interiors (ESI) 80NSSC20K0761. Michael West and Alex Fozkos were supported by the Office of State Seismologist of Alaska. This material is based on services provided by the GAGE Facility, operated by UNAVCO, Inc., with support from the National Science Foundation (NSF), the NASA, and the U.S. Geological Survey (USGS) under NSF Cooperative Agreement EAR-1724794. Incorporated Research Institutions for Seismology (IRIS) Data Services are funded through the Seismological Facilities for the Advancement of Geoscience (SAGE) Award of the NSF under Cooperative Support Agreement EAR-1851048. Seismic data were

recorded by the Alaska Earthquake Center under support from the USGS Advanced National Seismic System (ANSS) program cooperative agreement number G22AC00001 and retrieved via IRIS webservices. IRIS Data Services are funded through the SAGE Award of the NSF under Cooperative Support Agreement EAR-1851048.

## References

- Aster, R. C., B. Borchers, and C. H. Thurber (2018). *Parameter Estimation and Inverse Problems*, Second Ed., Elsevier Academic Press, Amsterdam, The Netherlands, 360 pp.
- Benedetti, E., M. Branzanti, L. Biagi, G. Colosimo, A. Mazzoni, and M. Crespi (2014). Global navigation satellite systems seismology for the 2012 Mw 6.1 Emilia earthquake: Exploiting the VADASE algorithm, *Seismol. Res. Lett.* **85**, no. 3, 649–656.
- Benz, H. M., M. Herman, A. C. Tarr, G. P. Hayes, K. P. Furlong, A. Villaseñor, R. L. Dart, and S. Rhea (2011). Seismicity of the earth 1900–2010 Aleutian arc and vicinity, *U.S. Geol. Surv. Open-File Rept. 2010-1083-B*, available at <https://pubs.usgs.gov/of/2010/1083/b/> (last accessed February 2023).
- Beyreuther, M., R. Barsch, L. Krischer, T. Megies, Y. Behr, and J. Wassermann (2010). ObsPy: A Python toolbox for seismology, *Seismol. Res. Lett.* **81**, no. 3, 530–533.
- Bock, Y., D. Melgar, and B. W. Crowell (2011). Real-time strong-motion broadband displacements from collocated GPS and accelerometers, *Bull. Seismol. Soc. Am.* **101**, no. 6, 2904–2925, doi: [10.1785/0120110007](https://doi.org/10.1785/0120110007).
- Colosimo, G., M. Crespi, and A. Mazzoni (2011). Real-time GPS seismology with a stand-alone receiver: A preliminary feasibility demonstration, *J. Geophys. Res.* **116**, no. 11, 1–14, doi: [10.1029/2010JB007941](https://doi.org/10.1029/2010JB007941).
- Crowell, B. W., and D. Melgar (2020). Slipping the Shumagin gap: A kinematic coseismic and early afterslip model of the Mw 7.8 Simeonof Island, Alaska, earthquake, *Geophys. Res. Lett.* **47**, no. 19, e2020GL090308, doi: [10.1029/2007JB005136](https://doi.org/10.1029/2007JB005136).
- Crowell, B. W., D. Melgar, Y. Bock, J. S. Haase, and J. Geng (2013). Earthquake magnitude scaling using seismogeodetic data, *Geophys. Res. Lett.* **40**, 6089–6094, doi: [10.1002/2013GL058391](https://doi.org/10.1002/2013GL058391).
- Crowell, B. W., D. A. Schmidt, P. Bodin, J. E. Vidale, J. Gombert, J. R. Hartog, V. C. Kress, T. I. Melbourne, M. Santillan, S. E. Minson, et al. (2016). Demonstration of the Cascadia G-FAST geodetic earthquake early warning system for the Nisqually, Washington, earthquake, *Seismol. Res. Lett.* **87**, no. 4, doi: [10.1785/0220150255](https://doi.org/10.1785/0220150255).
- Davies, J., L. Sykes, L. House, and K. Jacob (1981). Shumagin seismic gap, Alaska Peninsula: History of great earthquakes, tectonic setting, and evidence for high seismic potential, *J. Geophys. Res.* **86**, no. B5, 3821–3855.
- Drooff, C., and J. T. Freymueller (2021). New constraints on slip deficit on the Aleutian megathrust and inflation at Mt. Veniaminof, Alaska from repeat GPS measurements, *Geophys. Res. Lett.* **48**, no. 4, e2020GL091787, doi: [10.1029/2020GL091787](https://doi.org/10.1029/2020GL091787).
- Elliott, J. L., R. Grapenthin, R. M. Parameswaran, Z. Xiao, J. T. Freymueller, and L. Fusso (2022). Cascading rupture of a megathrust, *Sci. Adv.* **8**, no. 18, eabm4131, doi: [10.1126/sciadv.abm4131](https://doi.org/10.1126/sciadv.abm4131).
- Fang, R., J. Zheng, J. Geng, Y. Shu, C. Shi, and J. Liu (2020). Earthquake magnitude scaling using peak ground velocity derived from high-rate GNSS observations, *Seismol. Res. Lett.* **92**, no. 1, 227–237.
- Gaglione, S. (2015). How does a GNSS receiver estimate velocity? *Inside GNSS*, 38–41.
- Given, D. D., E. S. Cochran, T. H. Heaton, E. Hauksson, R. M. Allen, M. Hellweg, J. Vidale, and P. Bodin (2014). Technical implementation plan for the ShakeAlert production system: An earthquake early warning system for the West Coast of the United States, *U.S. Geol. Surv. Open-File Rept. 2014-1097*, 25 pp., doi: [10.3133/ofr20141097](https://doi.org/10.3133/ofr20141097).
- Grapenthin, R., I. A. Johanson, and R. M. Allen (2014a). Operational real-time GPS enhanced earthquake early warning, *J. Geophys. Res.* **119**, no. 10, 7944–7965, doi: [10.1002/2014JB011400](https://doi.org/10.1002/2014JB011400).
- Grapenthin, R., I. A. Johanson, and R. M. Allen (2014b). The 2014 Mw 6.0 Napa earthquake, California: Observations from real-time GPS-enhanced earthquake early warning, *Geophys. Res. Lett.* **41**, no. 23, 8269–8276, doi: [10.1002/2014GL061923](https://doi.org/10.1002/2014GL061923).
- Grapenthin, R., M. West, and J. Freymueller (2017). The utility of GNSS for earthquake early warning in regions with sparse seismic networks, *Bull. Seismol. Soc. Am.* **107**, no. 4, 1883–1890.
- Grapenthin, R., M. West, C. Tape, M. Gardine, and J. Freymueller (2018). Single-frequency instantaneous GNSS velocities resolve dynamic ground motion of the 2016 Mw 7.1 Iniskin, Alaska, earthquake, *Seismol. Res. Lett.* **89**, no. 3, 1040–1048.
- Ichinose, G., P. Somerville, H. K. Thio, R. Graves, and D. O'Connell (2007). Rupture process of the 1964 Prince William Sound, Alaska, earthquake from the combined inversion of seismic, tsunami, and geodetic data, *J. Geophys. Res.* **112**, no. B7, doi: [10.1029/2006JB004728](https://doi.org/10.1029/2006JB004728).
- Johnson, J. M., and K. Satake (1994). Rupture extent of the 1938 Alaskan earthquake as inferred from tsunami waveforms, *Geophys. Res. Lett.* **21**, no. 8, 733–736.
- Koketsu, K., H. Miyake, H. Fujiwara, and T. Hashimoto (2008). Progress towards a Japan integrated velocity structure model and long-period ground motion hazard map, *Proc. of the 14th World Conf. on Earthquake Engineering*, China Seismological Society, Beijing, China, S10–038.
- Krischer, L., A. Fichtner, S. Zukauskaitė, and H. Igel (2015). Large-scale seismic inversion framework, *Seismol. Res. Lett.* **86**, no. 4, 1198–1207.
- Kuyuk, H. S., R. M. Allen, H. Brown, M. Hellweg, I. Henson, and D. Neuhauser (2014). Designing a network-based earthquake early warning algorithm for California: ElarmS-2, *Bull. Seismol. Soc. Am.* **104**, no. 1, 162–173.
- Lewandowski, W., and E. F. Arias (2011). GNSS times and UTC, *Metrologia* **48**, no. 4, doi: [10.1088/0026-1394/48/4/S14](https://doi.org/10.1088/0026-1394/48/4/S14).
- Liu, C., T. Lay, and X. Xiong (2022). The 29 July 2021 MW 8.2 Chignik, Alaska Peninsula earthquake rupture inferred from seismic and geodetic observations: Re-Rupture of the Western 2/3 of the 1938 rupture zone, *Geophys. Res. Lett.* **49**, no. 4, e2021GL096004, doi: [10.1029/2021GL096004](https://doi.org/10.1029/2021GL096004).
- Liu, C., T. Lay, X. Xiong, and Y. Wen (2020). Rupture of the 2020  $M_w$  7.8 earthquake in the Shumagin gap inferred from seismic and geodetic observations, *Geophys. Res. Lett.* **47**, no. 22, e2020GL090806, doi: [10.1029/2020GL090806](https://doi.org/10.1029/2020GL090806).
- López, A. M., and E. A. Okal (2006). A seismological reassessment of the source of the 1946 Aleutian ‘tsunami’ earthquake, *Geophys. J. Int.* **165**, no. 3, 835–849.
- Megies, T., M. Beyreuther, R. Barsch, L. Krischer, and J. Wassermann (2011). ObsPy—What can it do for data centers and observatories? *Ann. Geophys.* **54**, no. 1, 47–58.
- Melgar, D., R. M. Allen, S. Riquelme, J. Geng, F. Bravo, J. C. Baez, H. Parra, S. Barrientos, P. Fang, Y. Bock, et al. (2016). Local tsunami

- warnings: Perspectives from recent large events, *Geophys. Res. Lett.* **43**, no. 3, 1109–1117, doi: [10.1002/2015GL067100](https://doi.org/10.1002/2015GL067100).
- Misra, P., and P. Enge (2011). *Global Positioning System: Signals, Measurements and Performance*, Second Ed., Ganga-Jamuna Press, 0970954425, 9780970954428, 569 pp.
- Morikawa, N., and H. Fujiwara (2013). A new ground motion prediction equation for Japan applicable up to M9 mega-earthquake, *J. Disaster Res.* **8**, no. 5, 878–888.
- Rinehart, A. J., S. A. McKenna, and T. A. Dewers (2016). Using wavelet covariance models for simultaneous picking of overlapping P- and S-wave arrival times in noisy single-component data, *Seismol. Res. Lett.* **87**, no. 4, 893–900.
- Stauder, W. (1968). Mechanism of the Rat Island earthquake sequence of February 4, 1965, with relation to island arcs and sea-floor spreading, *J. Geophys. Res.* **73**, no. 12, 3847–3858.
- Sykes, L. R., J. B. Kisslinger, L. House, J. N. Davies, and K. H. Jacob (1981). Rupture zones and repeat times of great earthquakes along the Alaska-Aleutian arc, 1784–1980, in *Earthquake Prediction: An International Review*, D. W. Simpson and P. G. Richards (Editors), Vol. 4, Maurice Ewing Series © American Geophysical Union, 73–80, doi: [10.1029/ME004p0073](https://doi.org/10.1029/ME004p0073).
- UNAVCO Community (2004a). PBO GPS Network - AB07-SandPoint\_AK2004 P.S., UNAVCO, *GPS/GNSS Observations Dataset*, doi: [10.7283/T59W0CDH](https://doi.org/10.7283/T59W0CDH).
- UNAVCO Community (2004b). PBO GPS Network - AC27-AC27MNeil\_AK2004 P.S., UNAVCO, *GPS/GNSS Observations Dataset*, doi: [10.7283/T5PR7T1N](https://doi.org/10.7283/T5PR7T1N).
- UNAVCO Community (2005). PBO GPS Network - AC25-King\_Cove\_AK2005 P.S., UNAVCO, *GPS/GNSS Observations Dataset*, doi: [10.7283/T5SF2T4X](https://doi.org/10.7283/T5SF2T4X).
- UNAVCO Community (2006a). PBO GPS Network - AB13-ChignikLgnAK2006 P.S., UNAVCO, *GPS/GNSS Observations Dataset*, doi: [10.7283/T5HQ3WW8](https://doi.org/10.7283/T5HQ3WW8).
- UNAVCO Community (2006b). PBO GPS Network - AC02-AkhiokCorpAK2005 P.S., UNAVCO, *GPS/GNSS Observations Dataset*, doi: [10.7283/T5Z60M01](https://doi.org/10.7283/T5Z60M01).
- UNAVCO Community (2006c). PBO GPS Network - AC21-PerryvilleAK2006 P.S., UNAVCO, *GPS/GNSS Observations Dataset*, doi: [10.7283/T5KK98RJ](https://doi.org/10.7283/T5KK98RJ).
- UNAVCO Community (2006d). PBO GPS Network - AC34-OldHarbor\_AK2006 P.S., UNAVCO, *GPS/GNSS Observations Dataset*, doi: [10.7283/T5028PG3](https://doi.org/10.7283/T5028PG3).
- UNAVCO Community (2006e). PBO GPS Network - AC39-ShuyakIsSPAK2006 P.S., UNAVCO, *GPS/GNSS Observations Dataset*, doi: [10.7283/T5TT4NX1](https://doi.org/10.7283/T5TT4NX1).
- UNAVCO Community (2006f). PBO GPS Network - AC41-PortMollerAK2006 P.S., UNAVCO, *GPS/GNSS Observations Dataset*, doi: [10.7283/T5FX77D3](https://doi.org/10.7283/T5FX77D3).
- UNAVCO Community (2006g). PBO GPS Network - AC45-SitkinakIsAK2006 P.S., UNAVCO, *GPS/GNSS Observations Dataset*, doi: [10.7283/T5J9NDC](https://doi.org/10.7283/T5J9NDC).
- UNAVCO Community (2006h). PBO GPS Network - AC67-PillarMtn\_AK2006 P.S., UNAVCO, *GPS/GNSS Observations Dataset*, doi: [10.7283/T5Q23X61](https://doi.org/10.7283/T5Q23X61).
- UNAVCO Community (2007a). PBO GPS Network - AB02-Nikolski\_AK2007 P.S., UNAVCO, *GPS/GNSS Observations Dataset*, doi: [10.7283/T5X63JX4](https://doi.org/10.7283/T5X63JX4).
- UNAVCO Community (2007b). PBO GPS Network - AB14-DillinghamAK2007 P.S., UNAVCO, *GPS/GNSS Observations Dataset*, doi: [10.7283/T5HT2M90](https://doi.org/10.7283/T5HT2M90).
- UNAVCO Community (2007c). PBO GPS Network - AC08-CapDouglasAK2007 P.S., UNAVCO, *GPS/GNSS Observations Dataset*, doi: [10.7283/T5HH6H21](https://doi.org/10.7283/T5HH6H21).
- UNAVCO Community (2007d). PBO GPS Network - AC40-PortHeidenAK2007 P.S., UNAVCO, *GPS/GNSS Observations Dataset*, doi: [10.7283/T50G3H4S](https://doi.org/10.7283/T50G3H4S).
- UNAVCO Community (2007e). PBO GPS Network - AC42-SanakIslandAK2007 P.S., UNAVCO, *GPS/GNSS Observations Dataset*, doi: [10.7283/T5VX0DJ1](https://doi.org/10.7283/T5VX0DJ1).
- UNAVCO Community (2007f). PBO GPS Network - AC47-SlopeMtn\_AK2007 P.S., UNAVCO, *GPS/GNSS Observations Dataset*, doi: [10.7283/T5N58JCI](https://doi.org/10.7283/T5N58JCI).
- UNAVCO Community (2007g). PBO GPS Network - AC52-PilotPointAK2007 P.S., UNAVCO, *GPS/GNSS Observations Dataset*, doi: [10.7283/T5ZP444C](https://doi.org/10.7283/T5ZP444C).
- UNAVCO Community (2008a). PBO GPS Network - AC26-Cape\_Gull\_AK2008 P.S., UNAVCO, *GPS/GNSS Observations Dataset*, doi: [10.7283/T58P5XJF](https://doi.org/10.7283/T58P5XJF).
- UNAVCO Community (2008b). PBO GPS Network - AC28-NagaiIslandAK2008 P.S., UNAVCO, *GPS/GNSS Observations Dataset*, doi: [10.7283/T53N21DV](https://doi.org/10.7283/T53N21DV).
- UNAVCO Community (2008c). PBO GPS Network - AC12-ChernaburaAK2008 P.S., UNAVCO, *GPS/GNSS Observations Dataset*, doi: [10.7283/T5NV9G7P](https://doi.org/10.7283/T5NV9G7P).
- UNAVCO Community (2008d). PBO GPS Network - AC13-ChirikofIsAK2008 P.S., UNAVCO, *GPS/GNSS Observations Dataset*, doi: [10.7283/T5F18WRV](https://doi.org/10.7283/T5F18WRV).
- Witter, R. C., R. W. Briggs, S. E. Engelhart, G. Gelfenbaum, R. D. Koehler, and W. D. Barnhart (2014). Little late Holocene strain accumulation and release on the Aleutian megathrust below the Shumagin Islands, Alaska, *Geophys. Res. Lett.* **41**, no. 7, 2359–2367.
- Worden, C. B., M. C. Gerstenberger, D. A. Rhoades, and D. J. Wald (2012). Probabilistic relationships between ground-motion parameters and modified Mercalli intensity in California, *Bull. Seismol. Soc. Am.* **102**, no. 1, 204–221.
- Wu, F. T., and H. Kanamori (1973). Source mechanism of February 4, 1965, Rat island earthquake, *J. Geophys. Res.* **78**, no. 26, 6082–6092.
- Xiao, Z., J. T. Freymueller, R. Grapenthin, J. L. Elliott, C. Drooff, and L. Fusso (2021). The deep Shumagin gap filled: Kinematic rupture model and slip budget analysis of the 2020 Mw 7.8 Simeonof earthquake constrained by GNSS, global seismic waveforms, and floating InSAR, *Earth Planet. Sci. Lett.* **576**, doi: [10.1016/j.epsl.2021.117241](https://doi.org/10.1016/j.epsl.2021.117241).
- Ye, L., Y. Bai, D. Si, T. Lay, K. F. Cheung, and H. Kanamori (2022). Rupture model for the 29 July 2021 MW 8.2 Chignik, Alaska earthquake constrained by seismic, geodetic, and tsunami observations, *J. Geophys. Res.* **127**, e2021JB023676, doi: [10.1029/2021JB023676](https://doi.org/10.1029/2021JB023676).
- Ye, L., T. Lay, H. Kanamori, Y. Yamazaki, and K. F. Cheung (2021). The 22 July 2020 Mw 7.8 Shumagin seismic gap earthquake: Partial rupture of a weakly coupled megathrust, *Earth Planet. Sci. Lett.* **562**, doi: [10.1016/j.epsl.2021.116879](https://doi.org/10.1016/j.epsl.2021.116879).

Manuscript received 8 November 2022

Published online 8 March 2023